


Effects of orbital selective dynamical correlation on the spin susceptibility and superconducting symmetries in Sr_2RuO_4

Chang-Youn Moon **Advanced Instrumentation Institute, Korea Research Institute of Standards and Science, Yuseong, Daejeon 305-340, Republic of Korea*

(Received 28 November 2022; revised 3 May 2023; accepted 9 May 2023; published 21 June 2023)

We investigate the connection between the local electron correlation and the momentum dependence of the spin susceptibility and the superconducting gap functions in Sr_2RuO_4 using density-functional theory combined with dynamical mean-field theory. Adopting a frequency-dependent two-particle vertex moves the zero-energy spin susceptibility peaks towards the Brillouin zone center, compared with the random-phase approximation, which basically retains the peak positions closer to the Brillouin zone boundary as determined by the Fermi-surface nesting. We find that the d_{xy} orbital plays a central role here via its enhanced correlation strength. Solving the linearized Eliashberg equation from this spin susceptibility, the prime candidates for the superconducting gap are an s -wave and a nearly degenerate d -wave solutions, all in the spin singlet. Furthermore, another set of degenerate spin-singlet gap functions emerges, odd with respect to the k point as well as orbital exchanges. We show that the stability of these gap functions is strongly dependent on the peak position of the spin susceptibility in the Brillouin zone.

DOI: [10.1103/PhysRevResearch.5.L022058](https://doi.org/10.1103/PhysRevResearch.5.L022058)

Sr_2RuO_4 remains one of the most intriguing superconductors with the possibility of highly exotic and unconventional superconductivity, even three decades after its discovery [1]. Noticing the analogy with superfluid ^3He , earlier studies kindled discussions of the $p_x + ip_y$ pairing [2–6]. This order parameter can be characterized by two essentially independent properties: the chirality, implying nonzero orbital magnetic moment, and the spin-triplet pairing. The spin-triplet pairing scenario, however, has come into serious question after recent spin susceptibility measurements using the nuclear magnetic resonance Knight shift [7,8] and polarized neutron scattering [9]. They showed that the susceptibility is suppressed below T_c , more consistent with the spin-singlet pairing, overruling an earlier contradicting Knight shift measurement [10]. The chirality, or time-reversal symmetry breaking (TRSB) more generally, has been supported by a recent zero-field muon spin relaxation (ZF- μ SR) measurement under uniaxial stress resulting in split superconducting and TRSB transitions [11], together with earlier works using ZF- μ SR [12] and nonzero Kerr rotation [13,14]. Evidence of the two-component order parameter [15,16] has also appeared and can serve as a broader constraint on the nature of pairing in which the possibility of the chirality is included. Combinations among even-parity order parameters such as s , d , and g symmetries are now generally considered plausible candidates.

The local electronic configuration near the Fermi energy E_F comprises four electrons in t_{2g} levels split from empty e_g levels within Ru d states, and hence, Sr_2RuO_4 is a multiorbital system in which Hund's coupling J_H plays a significant role in local Coulomb correlations. Consequently, its normal-state behaviors, such as the crossover from a high-temperature incoherent phase to a low-temperature Fermi liquid [2,17–22], are understood in the context of Hund's metals [23–26]. General features of Hund's metals include strong local spin fluctuation and orbital differentiation [27,28], as manifested in Sr_2RuO_4 with a much enhanced effective mass of the d_{xy} -derived Fermi-surface (FS) sheet compared with the $d_{xz/yz}$ -derived ones [2,23]. Then, an important question follows that how the local correlation which governs the normal state works on the superconductivity. Assuming spin-fluctuation-mediated superconductivity, the two-particle vertex, which forms fully interacting spin susceptibility χ when combined with the polarization bubble χ^0 , is one of the major channels through which the local correlation effect is incorporated in electron pairing. While some previous theoretical studies adopted the random-phase approximation (RPA) for the vertex with the lowest order scattering process [29–34], others found that using a frequency-dependent vertex produces qualitative differences in susceptibility and superconductivity [35–37]. However, the distinctive roles played by the orbital selectivity and its dynamic nature in the susceptibility evaluation remain elusive, especially with respect to the features critically connected to the pairing symmetry, such as the peak position of the susceptibility.

In this study, we demonstrate how the dynamic local correlations shape the susceptibility in k space and the pairing symmetry in Sr_2RuO_4 within the framework of density-functional theory combined with dynamical mean-field theory (DFT+DMFT). Adopting the dynamic vertex results in the peak position of spin susceptibility being closer to the

*cymoon@kriss.re.kr

Published by the American Physical Society under the terms of the [Creative Commons Attribution 4.0 International](https://creativecommons.org/licenses/by/4.0/) license. Further distribution of this work must maintain attribution to the author(s) and the published article's title, journal citation, and DOI.

Brillouin zone (BZ) center compared with the RPA case, in better agreement with experimental measurements. We argue it originates from the stronger frequency dependence of the vertex within the d_{xy} orbital than in the other t_{2g} components, relocating the peak from the position determined by simple FS nesting as in the RPA case. When the linearized Eliashberg equation is constructed from the susceptibility and solved, the most probable gap function turns out to be s -wave symmetry with nodes followed by a d -wave solution that is slightly less stable, suggesting a possible two-component order parameter with accidental degeneracy. Other plausible solutions are found to be symmetry-protected doubly degenerate ones which are odd with respect to both k and orbital exchanges. We show that the relative stability of these gap functions changes drastically between the respective susceptibility peak positions from the dynamical vertex and RPA, emphasizing the importance of an accurate evaluation of the susceptibility in k space and of the orbital selective and dynamic local correlation effects which enable it.

We use the modern implementation of the DFT+DMFT method within the all-electron embedded DMFT approach [38] which is based on WIEN2K [39], without downfolding or other approximations. The code is freely available on the web [40]. We employ the local-density approximation exchange-correlation functional [41,42], and the quantum impurity model is solved using the continuous-time quantum Monte Carlo impurity solver [43]. Here sampled quantities are expanded in the basis function obtained by the singular-value decomposition of the kernel for analytic continuation, ensuring reduced high-frequency noise [44]. Internal atomic positions are optimized, and $U = 4.5$ eV and $J = 1.0$ eV are adopted, consistent with a previous study on this material [45] employing the same computational method. We use the Slater parametrization of the Coulomb interaction in this study, and our U and J parameters are defined with respect to the three Slater parameters in such a way that $F^0 = U$, $F^2 = 112/13 J$, and $F^4 = 70/13 J$. BZ integration is done on the $30 \times 30 \times 30$ k -point mesh for the body-centered tetragonal primitive unit cell to obtain the converged charge density and self-energy, while a $40 \times 40 \times 2$ mesh in the BZ for the conventional tetragonal unit cell is used for the susceptibility and gap function calculations. All calculations are done at 116 K. Spin-orbit coupling (SOC) can have non-negligible effects on the electronic structure, mainly near the region where different sheets of FS intersect, via strong orbital mixing [46–50]. As evaluating the two-particle vertex including SOC is still not possible and also considering that susceptibilities are less affected by SOC than one-particle spectra [33], we neglect SOC in this work.

Figure 1(a) shows our calculated FS in the body-centered tetragonal BZ. Two one-dimensional (1D) FS sheets (α and β) are almost purely d_{xz} and d_{yz} derived, respectively, while the two-dimensional (2D) FS (γ) is from d_{xy} , consistent with previous studies. All local correlation effects as contained in the dynamical self-energy are included. Then we evaluate the susceptibility χ , the polarization bubble χ^0 , and the two-particle vertex Γ , which are related by the Bethe-Salpeter equation for a given bosonic Matsubara frequency Ω which is fixed to zero in this work: $\chi_{\alpha\alpha';\beta\beta'}^{s/c}(iv, iv', q) = \{[\chi^0(q)]^{-1} - \Gamma^{s/c}\}^{-1}_{\alpha\alpha';\beta\beta'}(iv, iv')$. All the two-particle quantities are defined

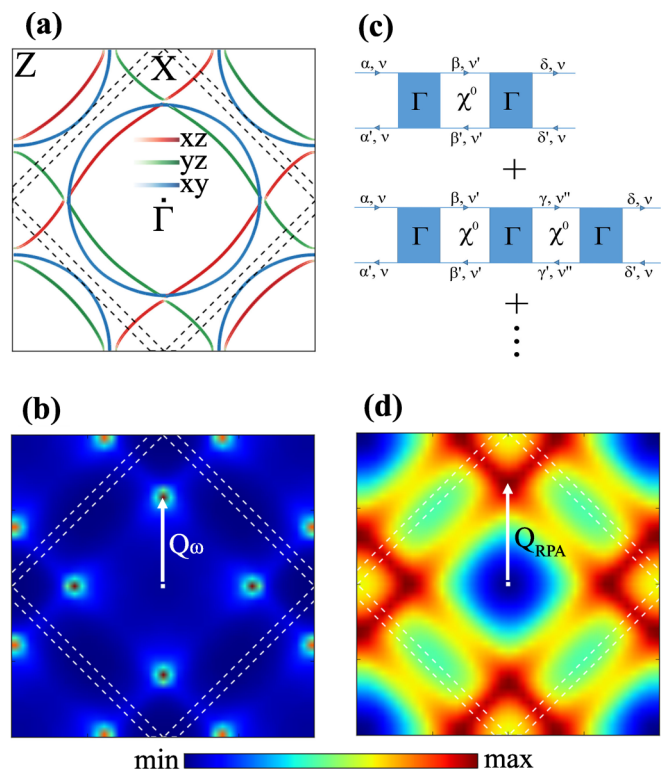


FIG. 1. (a) Fermi surface shown on the $k_z = 0$ plane. Orbital character is denoted by the depth of the color as well as the thickness of the line. (b) $[\Gamma \chi \Gamma]_{\alpha\alpha';\beta\beta'}^s(iv, iv)$, where $\alpha = d_{xy}$ and $iv \approx 0$ on the $k_z = 0$ plane. The momentum transfer of one of the four equivalent peaks inside the first Brillouin zone is marked by Q_ω . (c) Infinite series expansion of $[\Gamma \chi \Gamma]_{\alpha\alpha';\beta\beta'}^s(iv, iv)$ by the Bethe-Salpeter equation. Here the polarization bubble χ^0 is assumed to be diagonal in orbital indices (see the text). (d) Same as (b), but using the frequency-averaged constant two-particle vertex instead of the dynamic vertex. The peak is denoted by Q_{RPA} .

in the particle-hole channel if not explicitly indicated otherwise, and s/c stands for spin/charge. $\Gamma^{s/c}$ is a dynamic local quantity containing all two-particle-irreducible diagrams and is obtained in the impurity solver [51,52], as is the self-energy, which is the one-particle counterpart of the two-particle vertex. We display $\Gamma^s \chi^s \Gamma^s \equiv [\Gamma \chi \Gamma]^s$, which acts as an effective pairing potential in the Eliashberg equation, for the d_{xy} orbital channel at the lowest fermionic Matsubara frequency ($iv = iv' \approx 0$) [53] in Fig. 1(b). There is a strong peak at $q = (0.3, 0.3) \equiv Q_\omega$, where the X point is at $(0.5, 0.5)$, reproducing the peak position of χ from measurements [54] and previous calculations [36]. Note that $[\Gamma \chi \Gamma]^s$ has basically the same peak structure as χ^s in the BZ since the matrix multiplication between Γ^s and χ^s corresponds to the weighted summation over different frequency components of χ^s which have similar momentum structures to one another. To highlight the effect of the frequency dependence of the vertex, we evaluate $[\Gamma \chi \Gamma]^s$ in Fig. 1(d) using the frequency-averaged (static) vertex corresponding to the equal-time component, which is equivalent to RPA. The peak is now at $q = (0.35, 0.35) \equiv Q_{RPA}$, which is closer to X compared with Q_ω , also consistent with the previous calculation [36], suggesting that the momentum structure of the susceptibility alters with local

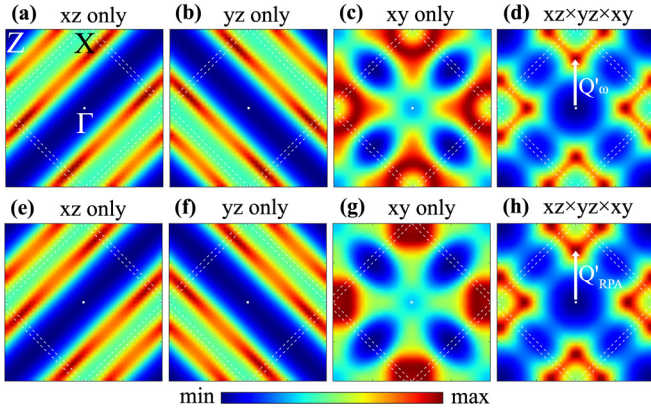


FIG. 2. With interorbital components of the vertex Γ set to zero, $[\Gamma\chi\Gamma]_{\alpha\alpha;\alpha\alpha}^s(i\nu \approx 0, i\nu \approx 0)$ is calculated for $\alpha = d_{xz/yz/xy}$ in (a)–(c). (e)–(g) are the same as (a)–(c), but with the frequency-averaged constant two-particle vertex instead of the dynamic vertex. (d) is obtained by multiplying (a), (b), and (c), while (h) is obtained by multiplying (e), (f), and (g). The peak position is denoted by $Q'_\omega/Q'_{\text{RPA}}$ in (d) and (h).

correlations with different dynamic structures. $d_{xz/yz}$ components have the same peak position as d_{xy} , but with a distinctively reduced amplitude, for both dynamic and static vertices where the orbital selectivity is inscribed. The charge counterpart, $[\Gamma\chi\Gamma]^c$, is found to be negligible compared with $[\Gamma\chi\Gamma]^s$ for the dynamic vertex, while they are comparable for the static vertex. See Appendix A for a detailed discussion of the orbital dependence of spin/charge susceptibilities.

Now we are ready to reveal the mechanism of how the orbital selectivity encoded in the local vertex determines the peak position of the susceptibility in k space. To help isolate the role of each orbital in its respective dynamic structure, we calculate $[\Gamma\chi\Gamma]^s$ with interorbital components of the vertex turned off, i.e., $\Gamma_{\alpha\alpha';\beta\beta'}^s = \Gamma_{\alpha\alpha';\alpha\alpha'}^s \delta_{\alpha,\beta} \delta_{\alpha',\beta'}$, and display the result in Fig. 2. Since the FSs are almost completely decoupled in orbitals, as seen in Fig. 1(a), the polarization bubble, defined as the product of two counterpropagating one-particle Green's functions, is also nearly diagonal: $\chi_{\alpha\alpha';\beta\beta'}^0(q) \approx \chi_{\alpha\alpha';\beta\beta'}^0(q) \delta_{\alpha,\beta} \delta_{\alpha',\beta'} \equiv \chi_{\alpha\alpha'}^0(q)$. Then $[\Gamma\chi\Gamma]_{\alpha\alpha;\alpha\alpha}^s(i\nu, i\nu', q)$ is mostly composed of $\chi_{\alpha\alpha}^0(i\nu'', q)$ with the weight of $\Gamma_{\alpha\alpha;\alpha\alpha}^s(i\nu'', i\nu''')$ for the intermediate frequencies $i\nu''$ and $i\nu'''$, but without incorporating orbital components other than α in the infinite series, as illustrated in Fig. 1(c). The diagonal component of $[\Gamma\chi\Gamma]^s$ in the d_{xz} orbital for $i\nu = i\nu' \approx 0$ is shown in Fig. 2(a). The stripe pattern along the x direction is from the FS nesting in the d_{xz} -originated 1D FS sheet, and the same is true for the d_{yz} component displayed in Fig. 2(b) with $\pi/2$ rotation. The fact that the k dependence of $[\Gamma\chi\Gamma]^s$ is determined by the simple FS nesting suggests that the vertex depends only weakly on the frequency, decoupling the polarization bubble from the vertex in the frequency domain for a given order of the infinite series in Fig. 1(c). Then the summation of the intermediate frequency produces $\sum_\nu \chi^0(i\nu) = \chi^0(\Omega = 0)$, the polarization bubble in zero bosonic frequency which is characterized by the FS nesting. Indeed, these results are almost identical to those from the frequency-averaged static vertex, as displayed

in Figs. 2(e) and 2(f). In the case of the d_{xy} channel, $[\Gamma\chi\Gamma]^s$ exhibits a fourfold rotation symmetry with weights around X points in the BZ reflecting the symmetry of the orbital, as shown in Figs. 2(c) and 2(g) for the dynamic and frequency-averaged static vertices, respectively. In contrast to the $d_{xz/yz}$ channels, however, there is a noticeable difference between the two vertices. Weights are distributed farther away from the Γ point for the dynamic vertex, which results from the frequency-dependent coefficient of $\chi^0(i\nu)$ (i.e., vertex) in the frequency ν summation, as elaborated in Appendix B.

As the next step, orbital-separate contributions shown in Figs. 2(a)–2(c) and 2(e)–2(g) can be effectively coupled again to reintroduce interorbital components in $[\Gamma\chi\Gamma]^s$ by simply multiplying the contributions from each orbital channel. This is because interorbital terms consisting of the product of χ^0 with different orbital indices, such as $\chi_{xy\ xy}^0 \chi_{xz\ xz}^0$, are restored by the multiplication in the infinite series expansion of $[\Gamma\chi\Gamma]^s$, as displayed in Fig. 1(c). Figures 2(d) and 2(h) are obtained by multiplying Figs. 2(a)–2(c) and 2(e)–2(g), respectively, and indeed reproduce the strong peak structure seen in the original full vertex calculation result in Figs. 1(b) and 1(d) which includes both intra- and interorbital components. Moreover, the peak position from the dynamic vertex in Fig. 2(d) at $Q'_\omega \approx (0.32, 0.32)$ is closer to the zone center than that from the static vertex at $Q'_{\text{RPA}} \approx (0.35, 0.35)$, also in accordance with the full vertex results. As we have demonstrated that $[\Gamma\chi\Gamma]^s$ can be effectively reconstructed from the product of orbital-separate components, it is evident that the difference in the peak position when using the dynamic and static vertices mainly originates from the contrasting weight distributions of the d_{xy} contribution: weight is distributed closer to the $\Gamma(X)$ point in Fig. 2(c) [Fig. 2(g)], resulting in the peak being closer to the $\Gamma(X)$ point in Fig. 2(d) [Fig. 2(h)]. Therefore, we can conclude that the d_{xy} component of the vertex is responsible for the shift of the peak position from $Q_{\text{RPA}} = (0.35, 0.35)$, as determined by the FS nesting, to $Q_\omega = (0.3, 0.3)$ via its strong frequency dependence. This is true not only for $\alpha = d_{xy}$ but also for $\alpha = d_{xz/yz}$ in $[\Gamma\chi\Gamma]_{\alpha\alpha;\alpha\alpha}^s$ (see Appendix A), which also incorporates $\chi_{xy\ xy}^0$ through the interorbital vertex. The pronounced dynamic nature of the d_{xy} component of the vertex is consistent with the d_{xy} orbital's larger mass enhancement factor, pointing to a larger correlation effect than $d_{xz/yz}$, which was suggested to originate from the proximity of the Van Hove singularity of the d_{xy} band to E_F [23].

Having calculated $[\Gamma\chi\Gamma]^{s/c}$, we can solve the linearized Eliashberg equation, which was also adopted in previous works [33,34,37,55], derived from the divergence condition of the susceptibility in the particle-particle channel:

$$-k_B T \sum_{k'v'\alpha'\beta'\gamma\delta} \Gamma_{\alpha\beta;\alpha'\beta'}^{pp,s/t}(k\nu; k'v') \chi_{\alpha'\beta'\gamma\delta}^{0,pp}(k'v') \Delta_{\gamma\delta}(k'v') = \lambda \Delta_{\alpha\beta}(k\nu),$$

where the eigenvalue λ and the eigenfunction Δ can be interpreted as the pairing strength and the gap function, respectively. $\Gamma^{pp,s/t}$ is the irreducible vertex in the particle-particle channel and consists of different combinations of $[\Gamma\chi\Gamma]^{s/c}$ in interchanged momentum and orbital indices depending on spin singlet/triplet (s/t) pairing. The details of

the formalism adopted in this study are given in Ref. [52]. Here we assume a constant frequency dependence of Γ^{PP} so that $\Gamma^{PP}(iv, iv') = \Gamma^{PP}(iv \approx 0, iv' \approx 0)$; then the resultant gap function $\Delta(k)$ does not depend on the frequency either, like in the BCS approximation, where only even-frequency solutions can be captured. Nevertheless, it should be noted that the internal frequency summations are performed without any approximation, which is found to be essential to obtain the correct peak position of $[\Gamma\chi\Gamma]^s$, as demonstrated above. The gap function so obtained is distributed over the entire BZ in the orbital basis and, in principle, at zero energy and hence needs to be projected to the FS, where the spectral function should be evaluated at zero energy:

$$\Delta_{ij}(k) = \sum_{\alpha\beta, i'j'} \Psi_{k,ii'}^L U_{k,i'\alpha} \Delta_{\alpha\beta}(k) U_{k,\beta j'}^\dagger \Psi_{k,j'j}^R.$$

Here $\Psi_{k,ii'}^{L(R)}$ is the i th left (right) eigenvector in the i' th DFT band basis of the complex DMFT eigenvalue equation at zero energy, and $U_{k,i'\alpha}$ is the projector between orbital α and the i' th DFT band at k [38,52]. This gives us more familiar gap functions that are similar to those defined in the band-based mean-field formalism instead of Green's functions. The gap functions for the three largest eigenvalues are displayed in Figs. 3(a)–3(c), all of which are in the spin singlet. The most probable solution with $\lambda = 0.0111$ is from the d_{xy} band and has the s -wave symmetry with nodes (“nodal s -wave,” A_{1g} irreducible representation), followed by a slightly less stable solution ($\lambda = 0.0101$) that also has the d_{xy} orbital character but in the $d_{x^2-y^2}$ symmetry (B_{1g} irreducible representation). Besides the symmetry-imposed nodes at the intersections between 2D and 1D FS sheets where the gap function changes the sign, there are also regions with depleted weights around the Van Hove point on the 2D FS for the $d_{x^2-y^2}$ solution. The proximity of the eigenvalues or the accidental (near) degeneracy between the s - and d -wave solutions points to the possibility of the TRSB $s + id$ order parameter suggested earlier [29–32], although it is $s + id_{xy}$ rather than $s + id_{x^2-y^2}$ that is more consistent with recent experiments [15,16,31]. Meanwhile, the third-largest eigenvalue ($\lambda = 0.0088$) is associated with doubly degenerate solutions which are protected by the lattice symmetry. Unlike s - and d -wave solutions which represent intraorbital (intraband) pairings within the d_{xy} orbital, the gap functions are interorbital between d_{xy} and $d_{xz/yz}$. One can see that the sign of the gap function is the opposite between d_{xy} and d_{xz} FSs where they meet, as in Fig. 3(c), indicating it is odd with respect to the orbital (band) interchange. Moreover, it is also odd in k space (f -wave, E_u irreducible representation), satisfying the antisymmetric fermion exchange rule [56]: $\hat{S}\hat{P}\hat{O}\hat{T} = -1 \times -1 \times -1 \times 1 = -1$. Odd-parity pairing, usually combined with a spin triplet, is here associated with the spin singlet, which is only possible with the extra degree of freedom of orbitals and hence is characteristic of the multiorbital superconductivity. A degenerate pair of gap functions, one from d_{xy} and d_{xz} and another from d_{xy} and d_{yz} [Fig. 3(c) and its $\pi/2$ rotation], can form a TRSB chiral order parameter $f + if$.

Our s -wave solution changes sign at every $\pi/4$ and hence is effectively stabilized by the repulsive pairing potential peaking at the smaller momentum transfer Q_ω compared with

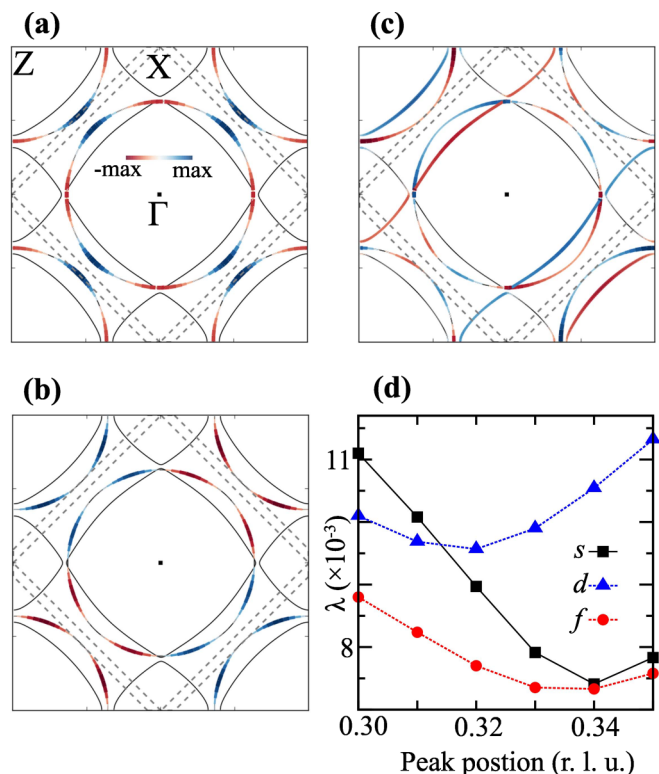


FIG. 3. Superconducting gap functions with the three largest eigenvalues from the linearized Eliashberg equation, projected to the DMFT band basis on the FS, all in the spin singlet. Gap functions in (a) and (b) are from the d_{xy} orbital with $\lambda = 0.0111$ and 0.0101 and with s - and d -wave symmetries, respectively. $\lambda = 0.0088$ solutions are doubly degenerate, where one has the interorbital gap function between d_{xz} and d_{xy} as shown in (c) and the other is between d_{yz} and d_{xy} with the gap function $\pi/2$ rotated from (c). These degenerate gap functions have odd-orbital and odd-parity f -wave symmetry. (d) Eigenvalue of each gap symmetry as a function of the peak position (q, q) in the spin susceptibility from Q_ω ($q = 0.30$) to Q_{RPA} ($q = 0.35$). The peak of the spin susceptibility in an arbitrary position is approximated by a Gaussian function centered at the position. Eigenvalues are rescaled so that they match the values from the original full calculation at Q_ω .

the longer Q_{RPA} determined by the FS nesting. Q_ω is rather short to connect the Van Hove regions with a higher density of states; hence, these regions are depleted in weight for the d -wave gap, making it a relatively less stable solution. Indeed, Mazin and Singh adopted susceptibility with a nesting-induced peak at $Q \approx (1/3, 1/3)$ to obtain a d -wave gap with maximum weights at the Van Hove point in their early work [57], while an s -wave gap has been suggested by using the peak position determined by inelastic neutron scattering at $Q \approx (0.3, 0.3)$ [54], consistent with our result. To explicitly study the relative stability of each solution with respect to the susceptibility peak position, we employ the spin susceptibility $[\Gamma\chi\Gamma]^s$ consisting of simple Gaussian peaks at any desired position in the BZ, which should be a reasonable approximation given the simple peak structures of the original spin susceptibility shown in Fig. 1(b). Solving the gap equation from this susceptibility consisting of Gaussian peaks, we display the result in Fig. 3(d). For s - and d -wave solutions, we

adopt $[\Gamma\chi\Gamma]^s$ with only the d_{xy} diagonal component, while for the f -wave gap only the interorbital components between d_{xy} and $d_{xz/yz}$ are set to be nonzero. The eigenvalue λ of each solution as a function of the peak position is rescaled so that it retains its original value from the full calculation at Q_ω . As expected, the s -wave gap grows unstable with increasing momentum transfer, while the d -wave gap is more stable at Q_{RPA} . The stability of the f -wave gap also decreases from Q_ω to Q_{RPA} , so that the d wave is dominant over other gap symmetries at Q_{RPA} . Therefore, we can conclude that TRSB $s + id$ and chiral $f + if$ gap symmetries are stabilized by the antiferromagnetic spin fluctuation near $Q_\omega = (0.3, 0.3)$, which is only available by using the dynamical vertex function.

Low-energy excitations and the presence of (vertical line) gap nodes are other requirements for the feasible gap symmetries imposed by experiments [58–63]. Our s - and d -wave solutions are from the d_{xy} FS, so the 1D FSs from $d_{xz/yz}$ are basically gapless for each of the two solutions [see Figs. 3(a) and 3(b)] and also for their TRSB complex combination $s + id$. When SOC is included, the d_{xy} component will be incorporated on the 1D FSs due to the orbital mixing, but it is likely that some part of 1D FSs is still gapless. On the other hand, the condition for the existence of gap nodes is tighter for the chiral $f + if$ order parameter since both 2D and 1D FSs participate in this interorbital electron pairing [Fig. 3(c) and its $\pi/2$ rotation]. Nevertheless, the Van Hove points in the 2D FS would have the least weight in the complex combination of a sign-changing node and the relatively smaller weight on the $\pi/2$ rotated point. Further studies might be required to elaborate on the compatibility of our suggested gap symmetries with experimental observations, as well as the possible effect of SOC [34,37].

In conclusion, we investigated the role of the dynamic local correlation in the spin susceptibility and the superconducting symmetry in Sr_2RuO_4 within the DFT+DMFT framework. The two-particle vertex was found to weakly depend on the frequency within $d_{xz/yz}$ orbitals, while its d_{xy} component is strongly frequency dependent, locating the peak of the spin susceptibility closer to the BZ center compared with the FS nesting-driven peak position. We found that the relatively smaller momentum transfer in the spin susceptibility stabilizes an s -wave gap with many sign-changing nodes, while it is against the stability of the d wave, resulting in an accidental near degeneracy of the two gap symmetries, both in the spin singlet. Odd-parity and odd-orbital f -wave spin-singlet gap functions were also found with symmetry-protected double degeneracy, which can lead to the realization of chiral superconductivity. Our work demonstrates how the local correlation and orbital selectivity in a Hund's metal affect the nonlocal electronic structure of the two-particle level and the superconductivity.

The author thanks Y. Bang, I. I. Mazin, E.-G. Moon, and K. Haule for helpful discussions. This work was supported by the Ministry of Science and ICT (Project Number: 2023-22030003-50) and Commercialization Promotion Agency for R&D Outcomes (COMPA).

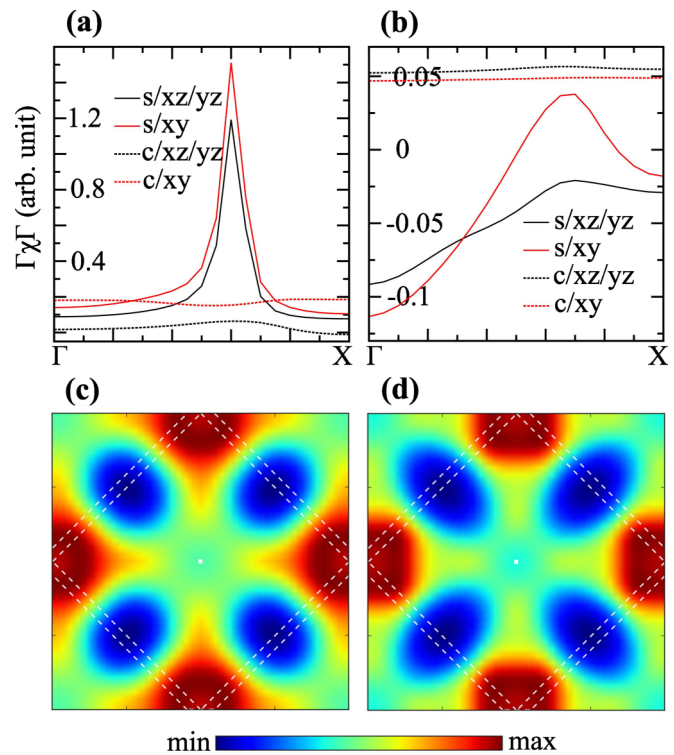


FIG. 4. (a) $[\Gamma\chi\Gamma]_{\alpha\alpha;\alpha\alpha}^{s/c}(i\nu, i\nu)$, where $\alpha = d_{xz/yz/xy}$ and $i\nu \approx 0$ along the Γ -X path in the Brillouin zone. s and c represent spin and charge. (b) Same as (a), but using the frequency-averaged constant two-particle vertex instead of the dynamic vertex. (c) $\sum_\nu c_\nu \chi^0(i\nu)$ in the d_{xy} orbital for the 10 lowest Matsubara frequencies, with a set of positive and negative coefficients c_ν for lower and higher frequencies, respectively. (d) Same as (c), but with a constant c_ν .

APPENDIX A: ORBITAL, SPIN/CHARGE, AND VERTEX DEPENDENCE OF $\Gamma\chi\Gamma$

The $\alpha = d_{xz/yz}$ components of $[\Gamma\chi\Gamma]_{\alpha\alpha;\alpha\alpha}^s$ have the same peak position as $\alpha = d_{xy}$, but with distinctively reduced amplitudes for both the dynamic and static vertices, as shown in Figs. 4(a) and 4(b), respectively. This feature results from the orbital selectivity in Sr_2RuO_4 , a Hund's metal, as inscribed in both of our vertices but not in a simple RPA in which all orbitals are treated the same. Another hallmark of Hund's metals is the contrast between fast fluctuating charge due to the reduced interorbital charge repulsion and slow spin fluctuation with strong Hund's coupling or a large difference in the coherence temperatures between charge and spin [26–28,64–66]. This feature can readily be seen with the much suppressed charge fluctuation in Fig. 4(a), as estimated at the lowest energy, owing to the dynamic nature of the vertex. It indicates that the superconductivity is mainly determined by the spin fluctuation, while the contribution of the charge fluctuation is not significant in Sr_2RuO_4 . In the case of our static vertex, unlike a conventional RPA using the same single parameters U , U' , and J for all orbitals, the orbital differentiation between the xy and xz/yz orbitals is still present in this level of approximation, as can be seen in Fig. 4(b) for the spin fluctuation. Meanwhile, the charge fluctuation is found to

be almost comparable in size to the spin fluctuation for the static vertex in Fig. 4(b), implying that the separation of the spin-charge coherence scales fails to emerge using a static vertex. Consequently, this suggests that both charge and spin fluctuations contribute to the superconductivity within static vertex approximations, including RPA.

APPENDIX B: DIFFERENCE BETWEEN USING DYNAMIC AND STATIC d_{xy} -DIAGONAL VERTICES IN $[\Gamma\chi\Gamma]^s$

$[\Gamma\chi\Gamma]^s_{\alpha\alpha;\alpha\alpha}$ calculated using an orbital-diagonal (interorbital scattering is prohibited) vertex in d_{xy} exhibits considerable difference between the dynamic and static vertices,

as shown in Figs. 2(c) and 2(g), respectively. Here we demonstrate how the constant (static vertex) and frequency-dependent (dynamic vertex) coefficients of $\chi^0(i\nu)$ in the frequency summation cause that difference, using only a small number of frequencies. Figure 4(d) is obtained by adding the first 10 Matsubara frequency components of $\chi^0(i\nu)$ with a constant coefficient, reproducing most of the features in Fig. 2(g) from the summation of a much larger number of frequencies. On the other hand, we need a set of positive coefficients at lower energies and negative coefficients at higher energies among the 10 Matsubara frequencies in the $\chi^0(i\nu)$ summation to obtain Fig. 4(c), which also captures the feature of weights distributed closer to the Γ point, as shown in Fig. 2(c).

-
- [1] Y. Maeno, H. Hashimoto, K. Yoshida, S. Nishizaki, T. Fujita, J. G. Bednorz, and F. Lichtenberg, Superconductivity in a layered perovskite without copper, *Nature (London)* **372**, 532 (1994).
- [2] A. P. Mackenzie and Y. Maeno, The superconductivity of Sr_2RuO_4 and the physics of spin-triplet pairing, *Rev. Mod. Phys.* **75**, 657 (2003).
- [3] T. M. Rice and M. Sigrist, Sr_2RuO_4 : An electronic analogue of ^3He ?, *J. Phys.: Condens. Matter* **7**, L643 (1995).
- [4] M. Sigrist, Ehrenfest relations for ultrasound absorption in Sr_2RuO_4 , *Prog. Theor. Phys.* **107**, 917 (2002).
- [5] Y. Maeno, S. Kittaka, T. Nomura, S. Yonezawa, and K. Ishida, Evaluation of spin-triplet superconductivity in Sr_2RuO_4 , *J. Phys. Soc. Jpn.* **81**, 011009 (2012).
- [6] C. Kallin, Chiral p-wave order in Sr_2RuO_4 , *Rep. Prog. Phys.* **75**, 042501 (2012).
- [7] A. Pustogow, Y. Luo, A. Chronister, Y. S. Su, D. A. Sokolov, F. Jerzembeck, A. P. Mackenzie, C. W. Hicks, N. Kikugawa, S. Raghu, E. D. Bauer, and S. E. Brown, Constraints on the superconducting order parameter in Sr_2RuO_4 from oxygen-17 nuclear magnetic resonance, *Nature (London)* **574**, 72 (2019).
- [8] K. Ishida, M. Manago, K. Kinjo, and Y. Maeno, Reduction of the ^{17}O Knight shift in the superconducting state and the heat-up effect by NMR pulses on Sr_2RuO_4 , *J. Phys. Soc. Jpn.* **89**, 034712 (2020).
- [9] A. N. Petsch, M. Zhu, M. Enderle, Z. Q. Mao, Y. Maeno, I. I. Mazin, and S. M. Hayden, Reduction of the Spin Susceptibility in the Superconducting State of Sr_2RuO_4 Observed by Polarized Neutron Scattering, *Phys. Rev. Lett.* **125**, 217004 (2020).
- [10] K. Ishida, H. Mukuda, Y. Kitaoka, K. Asayama, Z. Q. Mao, Y. Mori, and Y. Maeno, Spin-triplet superconductivity in Sr_2RuO_4 identified by ^{17}O Knight shift, *Nature (London)* **396**, 658 (1998).
- [11] V. Grinenko, S. Ghosh, R. Sarkar, J.-C. Orain, A. Nikitin, M. Elender, D. Das, Z. Guguchia, F. Bruckner, M. E. Barber, J. Park, N. Kikugawa, D. A. Sokolov, J. S. Bobowski, T. Miyoshi, Y. Maeno, A. P. Mackenzie, H. Luetkens, C. W. Hicks, and H.-H. Klauss, Split superconducting and time-reversal symmetry-breaking transitions in Sr_2RuO_4 under stress, *Nat. Phys.* **17**, 748 (2021).
- [12] G. M. Luke, Y. Fudamoto, K. M. Kojima, M. I. Larkin, J. Merrin, B. Nachumi, Y. J. Uemura, Y. Maeno, Z. Q. Mao, Y. Mori, H. Nakamura, and M. Sigrist, Time-reversal symmetry-breaking superconductivity in Sr_2RuO_4 , *Nature (London)* **394**, 558 (1998).
- [13] J. Xia, Y. Maeno, P. T. Beyersdorf, M. M. Fejer, and A. Kapitulnik, High Resolution Polar Kerr Effect Measurements of Sr_2RuO_4 : Evidence for Broken Time-Reversal Symmetry in the Superconducting State, *Phys. Rev. Lett.* **97**, 167002 (2006).
- [14] A. Kapitulnik, J. Xia, E. Schemm, and A. Palevski, Polar Kerr effect as probe for time-reversal symmetry breaking in unconventional superconductors, *New J. Phys.* **11**, 055060 (2009).
- [15] S. Benhabib, C. Lupien, I. Paul, L. Berges, M. Dion, M. Nardone, A. Zitouni, Z. Q. Mao, Y. Maeno, A. Georges, L. Taillefer, and C. Proust, Ultrasound evidence for a two-component superconducting order parameter in Sr_2RuO_4 , *Nat. Phys.* **17**, 194 (2021).
- [16] S. Ghosh, A. Shekhter, F. Jerzembeck, N. Kikugawa, D. A. Sokolov, M. Brando, A. P. Mackenzie, C. W. Hicks, and B. J. Ramshaw, Thermodynamic evidence for a two-component superconducting order parameter in Sr_2RuO_4 , *Nat. Phys.* **17**, 199 (2021).
- [17] T. Katsufuji, M. Kasai, and Y. Tokura, In-Plane and Out-of-Plane Optical Spectra of Sr_2RuO_4 , *Phys. Rev. Lett.* **76**, 126 (1996).
- [18] T. Imai, A. W. Hunt, K. R. Thurber, and F. C. Chou, ^{17}O NMR Evidence for Orbital Dependent Ferromagnetic Correlations in Sr_2RuO_4 , *Phys. Rev. Lett.* **81**, 3006 (1998).
- [19] N. E. Hussey, A. P. Mackenzie, J. R. Cooper, Y. Maeno, S. Nishizaki, and T. Fujita, Normal-state magnetoresistance of Sr_2RuO_4 , *Phys. Rev. B* **57**, 5505 (1998).
- [20] T. Valla, P. D. Johnson, Z. Yusof, B. Wells, Q. Li, S. M. Loureiro, R. J. Cava, M. Mikami, Y. Mori, M. Yoshimura, and T. Sasaki, Coherence–incoherence and dimensional crossover in layered strongly correlated metals, *Nature (London)* **417**, 627 (2002).
- [21] S.-C. Wang, H.-B. Yang, A. K. P. Sekharan, H. Ding, J. R. Engelbrecht, X. Dai, Z. Wang, A. Kaminski, T. Valla, T. Kidd, A. V. Fedorov, and P. D. Johnson, Quasiparticle Line Shape of Sr_2RuO_4 and Its Relation to Anisotropic Transport, *Phys. Rev. Lett.* **92**, 137002 (2004).
- [22] T. E. Kidd, T. Valla, A. V. Fedorov, P. D. Johnson, R. J. Cava, and M. K. Haas, Orbital Dependence of the Fermi Liquid State in Sr_2RuO_4 , *Phys. Rev. Lett.* **94**, 107003 (2005).

- [23] J. Mravlje, M. Aichhorn, T. Miyake, K. Haule, G. Kotliar, and A. Georges, Coherence-Incoherence Crossover and the Mass-Renormalization Puzzles in Sr_2RuO_4 , *Phys. Rev. Lett.* **106**, 096401 (2011).
- [24] L. de' Medici, J. Mravlje, and A. Georges, Janus-Faced Influence of Hund's Rule Coupling in Strongly Correlated Materials, *Phys. Rev. Lett.* **107**, 256401 (2011).
- [25] J. Mravlje and A. Georges, Thermopower and Entropy: Lessons from Sr_2RuO_4 , *Phys. Rev. Lett.* **117**, 036401 (2016).
- [26] F. B. Kugler, M. Zingl, H. U. R. Strand, S.-S. B. Lee, J. von Delft, and A. Georges, Strongly Correlated Materials from a Numerical Renormalization Group Perspective: How the Fermi-Liquid State of Sr_2RuO_4 Emerges, *Phys. Rev. Lett.* **124**, 016401 (2020).
- [27] K. Haule and G. Kotliar, Coherence-incoherence crossover in the normal state of iron oxypnictides and importance of Hund's rule coupling, *New J. Phys.* **11**, 025021 (2009).
- [28] C.-Y. Moon, Strong enhancement of magnetic order from bulk to stretched monolayer FeSe as Hund's metals, *npj Comput. Mater.* **6**, 147 (2020).
- [29] A. T. Romer, D. D. Scherer, I. M. Eremin, P. J. Hirschfeld, and B. M. Andersen, Knight Shift and Leading Superconducting Instability from Spin Fluctuations in Sr_2RuO_4 , *Phys. Rev. Lett.* **123**, 247001 (2019).
- [30] A. T. Romer, A. Kreisel, M. A. Muller, P. J. Hirschfeld, I. M. Eremin, and B. M. Andersen, Theory of strain-induced magnetic order and splitting of T_c and T_{TRSB} in Sr_2RuO_4 , *Phys. Rev. B* **102**, 054506 (2020).
- [31] A. T. Romer, P. J. Hirschfeld, and B. M. Andersen, Superconducting state of Sr_2RuO_4 in the presence of longer-range Coulomb interactions, *Phys. Rev. B* **104**, 064507 (2021).
- [32] A. T. Romer, T. A. Maier, A. Kreisel, P. J. Hirschfeld, and B. M. Andersen, Leading superconducting instabilities in three-dimensional models for Sr_2RuO_4 , *Phys. Rev. Res.* **4**, 033011 (2022).
- [33] O. Gingras, R. Nourafkan, A.-M. S. Tremblay, and M. Cote, Superconducting Symmetries of Sr_2RuO_4 from First-Principles Electronic Structure, *Phys. Rev. Lett.* **123**, 217005 (2019).
- [34] O. Gingras, N. Allaglo, R. Nourafkan, M. Cote, and A.-M. S. Tremblay, Superconductivity in correlated multiorbital systems with spin-orbit coupling: Coexistence of even- and odd-frequency pairing, and the case of Sr_2RuO_4 , *Phys. Rev. B* **106**, 064513 (2022).
- [35] L. Boehnke, P. Werner, and F. Lechermann, Multi-orbital nature of the spin fluctuations in Sr_2RuO_4 , *Europhys. Lett.* **122**, 57001 (2018).
- [36] H. U. R. Strand, M. Zingl, N. Wentzell, O. Parcollet, and A. Georges, Magnetic response of Sr_2RuO_4 : Quasi-local spin fluctuations due to Hund's coupling, *Phys. Rev. B* **100**, 125120 (2019).
- [37] S. Käser, H. U. R. Strand, N. Wentzell, A. Georges, O. Parcollet, and P. Hansmann, Interorbital singlet pairing in Sr_2RuO_4 : A Hund's superconductor, *Phys. Rev. B* **105**, 155101 (2022).
- [38] K. Haule, C.-H. Yee, and K. Kim, Dynamical mean-field theory within the full-potential methods: Electronic structure of CeIrIn_5 , CeCoIn_5 , and CeRhIn_5 , *Phys. Rev. B* **81**, 195107 (2010).
- [39] P. Blaha, K. Schwarz, G. Madsen, D. Kvasnicka, and J. Luitz, *WIEN2k* (Vienna University of Technology, Vienna, 2001).
- [40] <http://hauleweb.rutgers.edu/tutorials/>.
- [41] D. M. Ceperley, and B. J. Alder, Ground State of the Electron Gas by a Stochastic Method, *Phys. Rev. Lett.* **45**, 566 (1980).
- [42] J. P. Perdew and Y. Wang, Accurate and simple analytic representation of the electron-gas correlation energy, *Phys. Rev. B* **45**, 13244 (1992).
- [43] K. Haule, Quantum Monte Carlo impurity solver for cluster dynamical mean-field theory and electronic structure calculations with adjustable cluster base, *Phys. Rev. B* **75**, 155113 (2007).
- [44] H. Shinaoka, J. Otsuki, K. Haule, M. Wallerberger, E. Gull, K. Yoshimi, and M. Ohzeki, Overcomplete compact representation of two-particle Green's functions, *Phys. Rev. B* **97**, 205111 (2018).
- [45] X. Deng, K. Haule, and G. Kotliar, Transport Properties of Metallic Ruthenates: A DFT+DMFT Investigation, *Phys. Rev. Lett.* **116**, 256401 (2016) For detailed information on the Coulomb parametrization employed in this work, refer to <http://hauleweb.rutgers.edu/tutorials/CoulombUexplain.html>.
- [46] M. W. Haverkort, I. S. Elfimov, L. H. Tjeng, G. A. Sawatzky, and A. Damascelli, Strong Spin-Orbit Coupling Effects on the Fermi Surface of Sr_2RuO_4 and Sr_2RhO_4 , *Phys. Rev. Lett.* **101**, 026406 (2008).
- [47] C. N. Veenstra, Z.-H. Zhu, M. Raichle, B. M. Ludbrook, A. Nicolaou, B. Slomski, G. Landolt, S. Kittaka, Y. Maeno, J. H. Dil, I. S. Elfimov, M. W. Haverkort, and A. Damascelli, Spin-Orbital Entanglement and the Breakdown of Singlets and Triplets in Sr_2RuO_4 Revealed by Spin- and Angle-Resolved Photoemission Spectroscopy, *Phys. Rev. Lett.* **112**, 127002 (2014).
- [48] G. Zhang, E. Gorelov, E. Sarvestani, and E. Pavarini, Fermi Surface of Sr_2RuO_4 : Spin-Orbit and Anisotropic Coulomb Interaction Effects, *Phys. Rev. Lett.* **116**, 106402 (2016).
- [49] M. Kim, J. Mravlje, M. Ferrero, O. Parcollet, and A. Georges, Spin-Orbit Coupling and Electronic Correlations in Sr_2RuO_4 , *Phys. Rev. Lett.* **120**, 126401 (2018).
- [50] A. Tamai, M. Zingl, E. Rozbicki, E. Cappelli, S. Ricco, A. de la Torre, S. McKeown Walker, F. Y. Bruno, P. D. C. King, W. Meevasana, M. Shi, M. Radovi, N. C. Plumb, A. S. Gibbs, A. P. Mackenzie, C. Berthod, H. U. R. Strand, M. Kim, A. Georges, and F. Baumberger, High-Resolution Photoemission on Sr_2RuO_4 Reveals Correlation-Enhanced Effective Spin-Orbit Coupling and Dominantly Local Self-Energies, *Phys. Rev. X* **9**, 021048 (2019).
- [51] H. Park, K. Haule, and G. Kotliar, Magnetic Excitation Spectra in BaFe_2As_2 : A Two-Particle Approach within a Combination of the Density Functional Theory and the Dynamical Mean-Field Theory Method, *Phys. Rev. Lett.* **107**, 137007 (2011).
- [52] Z. P. Yin, K. Haule, and G. Kotliar, Spin dynamics and orbital-antiphase pairing symmetry in iron-based superconductors, *Nat. Phys.* **10**, 845 (2014).
- [53] Because of the slight difference between the value at $i\nu = i\nu' = 0^\pm$ and that at $i\nu = -i\nu' = 0^\pm$, where $0^{+(\pm)}$ represents the first positive (negative) fermionic Matsubara frequency, we take the average between the two values. The same is true throughout this paper whenever this notation appears.
- [54] P. Steffens, Y. Sidis, J. Kulda, Z. Q. Mao, Y. Maeno, I. I. Mazin, and M. Braden, Spin Fluctuations in Sr_2RuO_4 from Polarized

- Neutron Scattering: Implications for Superconductivity, *Phys. Rev. Lett.* **122**, 047004 (2019).
- [55] S. Acharya, D. Pashov, C. Weber, H. Park, L. Sponza, and M. V. Schilfgaarde, Evening out the spin and charge parity to increase T_c in Sr_2RuO_4 , *Commun. Phys.* **2**, 163 (2019).
- [56] J. Linder and A. V. Balatsky, Odd-frequency superconductivity, *Rev. Mod. Phys.* **91**, 045005 (2019).
- [57] I. I. Mazin and D. J. Singh, Competitions in Layered Ruthenates: Ferromagnetism versus Antiferromagnetism and Triplet versus Singlet Pairing, *Phys. Rev. Lett.* **82**, 4324 (1999).
- [58] I. Bonalde, B. D. Yanoff, M. B. Salamon, D. J. Van Harlingen, E. M. E. Chia, Z. Q. Mao, and Y. Maeno, Temperature Dependence of the Penetration Depth in Sr_2RuO_4 : Evidence for Nodes in the Gap Function, *Phys. Rev. Lett.* **85**, 4775 (2000).
- [59] K. Izawa, H. Takahashi, H. Yamaguchi, Y. Matsuda, M. Suzuki, T. Sasaki, T. Fukase, Y. Yoshida, R. Settai, and Y. Onuki, Superconducting Gap Structure of Spin-Triplet Superconductor Sr_2RuO_4 Studied by Thermal Conductivity, *Phys. Rev. Lett.* **86**, 2653 (2001).
- [60] I. A. Firmo, S. Lederer, C. Lupien, A. P. Mackenzie, J. C. Davis, and S. A. Kivelson, Evidence from tunneling spectroscopy for a quasi-one-dimensional origin of superconductivity in Sr_2RuO_4 , *Phys. Rev. B* **88**, 134521 (2013).
- [61] E. Hassinger, P. Bourgeois-Hope, H. Taniguchi, S. Rene de Cotret, G. Grissonnanche, M. S. Anwar, Y. Maeno, N. Doiron-Leyraud, and L. Taillefer, Vertical Line Nodes in the Superconducting Gap Structure of Sr_2RuO_4 , *Phys. Rev. X* **7**, 011032 (2017).
- [62] S. Kittaka, S. Nakamura, T. Sakakibara, N. Kikugawa, T. Terashima, S. Uji, D. A. Sokolov, A. P. Mackenzie, K. Irie, Y. Tsutsumi, K. Suzuki, and K. Machida, Searching for gap zeros in Sr_2RuO_4 via field-angle-dependent specific-heat measurement, *J. Phys. Soc. Jpn.* **87**, 093703 (2018).
- [63] R. Sharma, S. D. Edkins, Z. Wang, A. Kostin, C. Sow, Y. Maeno, A. P. Mackenzie, J. C. S. Davis, and V. Madhavan, Momentum-resolved superconducting energy gaps of Sr_2RuO_4 from quasiparticle interference imaging, *Proc. Natl. Acad. Sci. USA* **117**, 5222 (2020).
- [64] Z. P. Yin, K. Haule, and G. Kotliar, Kinetic frustration and the nature of the magnetic and paramagnetic states in iron pnictides and iron chalcogenides, *Nat. Mater.* **10**, 932 (2011).
- [65] Z. P. Yin, K. Haule, and G. Kotliar, Magnetism and charge dynamics in iron pnictides, *Nat. Phys.* **7**, 294 (2011).
- [66] L. Fanfarillo and E. Bascones, Electronic correlations in Hund metals, *Phys. Rev. B* **92**, 075136 (2015).